

Article

What Is the Nature of Supramolecular Bonding? Comprehensive NBO/NRT Picture of Halogen and Pnictogen Bonding in $RPH_2 \cdots IF/FI$ Complexes ($R = CH_3, OH, CF_3, CN, NO_2$)

Yinchun Jiao ¹ and Frank Weinhold ^{2,*}

¹ Key Laboratory of Theoretical Organic Chemistry and Functional Molecules, Ministry of Education, School of Chemistry and Chemical Engineering, Hunan University of Science and Technology, Xiangtan 411201, China; jiao28@wisc.edu

² Theoretical Chemistry Institute and Department of Chemistry, University of Wisconsin-Madison, Madison, WI 53706, USA

* Correspondence: weinhold@chem.wisc.edu

Academic Editor: Antonio Caballero

Received: 14 May 2019; Accepted: 30 May 2019; Published: 31 May 2019



Abstract: We employ a variety of natural bond orbital (NBO) and natural resonance theory (NRT) tools to comprehensively investigate the nature of halogen and pnictogen bonding interactions in $RPH_2 \cdots IF/FI$ binary complexes ($R = CH_3, OH, CF_3, CN, \text{ and } NO_2$) and the tuning effects of R-substituents. Though such interactions are commonly attributed to “sigma-hole”-type electrostatic effects, we show that they exhibit profound similarities and analogies to the resonance-type 3-center, 4-electron (3c/4e) donor-acceptor interactions of hydrogen bonding, where classical-type “electrostatics” are known to play only a secondary modulating role. The general 3c/4e resonance perspective corresponds to a continuous range of interatomic $A \cdots B$ bond orders (b_{AB}), spanning both the stronger “covalent” interactions of the molecular domain (say, $b_{AB} \geq \frac{1}{2}$) and the weaker interactions ($b_{AB} < \frac{1}{2}$, often misleadingly termed “noncovalent”) that underlie supramolecular complexation phenomena. We show how a unified NBO/NRT-based description of hydrogen, halogen, pnictogen, and related bonding yields an improved predictive utility and intuitive understanding of empirical trends in binding energies, structural geometry, and other measurable properties that are expected to be manifested in all such supramolecular interaction phenomena.

Keywords: supramolecular bonding; halogen bond; pnictogen bond; hydrogen bond; natural bond orbital; natural resonance theory; fractional bond order; resonance theory

1. Introduction

Recent computational [1–4] and experimental [5–8] studies have called attention to the multiplicity of halogen [9–13], chalcogen [14,15], pnictogen [16], and tetrel bonds [17–19] (corresponding to Groups 17, 16, 15, and 14, respectively) that appear necessary to supplement the familiar hydrogen bonds of intermolecular interaction theory [20]. Such proliferating “bond” forms naturally reignite age-old controversies concerning the relative importance of “covalent” versus “electrostatic” contributions in the general theory of intermolecular forces [21–24]. Of course, all protagonists concur that the only relevant potential terms in the non-relativistic Hamiltonian are of Coulombic form (hence, tautologically “electrostatic” in nature). However, the deeper issue is whether supramolecular complexation (like molecule formation) is primarily governed by exchange-type (exponential) interactions of the short-range quantal regime or by the exchange-free (power-law) behavior of the long-range classical limit. In short, we ask whether orbital-based (quantal) or “dipole–dipole”-type (classical) conceptions

basis levels discussed below) as well as opposite in sign to that expected for the authentic London dispersion attraction (acting instead to reduce ΔE_{bind}). Such “corrections” are not considered further in the present work.

In the following, we first describe the species, computational levels, and NBO/NRT methods to be employed. The latter include NBO $\Delta E^{(2)}_{n\sigma^*}$, charge–transfer $Q_{n\sigma^*}$, and \$DEL-deletion $\Delta E^{\text{\$DEL}}_{n\sigma^*}$ measures of donor–acceptor attraction [49], the corresponding pairwise steric-exchange opposition ($\Delta E^{(\text{pw})}_{n\sigma}$) of filled orbitals [54] that completes the 3c/4e description of overall bonding energetics, and the various NRT-based regularities and correlations with measurable properties that are considered diagnostic of H-bonding [22]. We then document the systematic application of these NBO/NRT methods to the title species to exhibit their mutual coherence and consistency with well-established features of H-bonding. The concluding summary emphasizes how a balanced NBO/NRT description of leading donor–acceptor interactions can lead to a unified conceptual picture of supramolecular bonding that encompasses the entire range of chemically significant (“non-innocent”) complexation and ligation phenomena.

2. Computational Methods and Results

Our studies began with a larger data set of dihalogen complexes $\text{RPH}_2\cdots\text{XY}$ that included all possible ($X, Y = \text{F, Cl, Br, I}$) dihalogen species of the first four periodic rows. However, from a qualitative conceptual perspective, it soon became apparent that the properties of such complexes vary in a smooth and chemically reasonable fashion with dihalogen polarity, as maximized in the iodine–fluorine (IF) species. Accordingly, we focus here on the “polar extremes” of $\text{RPH}_2\cdots\text{IF}$ versus $\text{RPH}_2\cdots\text{FI}$ complexation, corresponding to opposed signs of any envisioned “dipole–dipole” contributions to intermolecular binding. A direct comparison of these two extremes thereby allows one to recognize the important modulating influence of classical dipole–dipole forces (i.e., in strengthening or weakening the underlying quantal interactions), while also verifying that resonance-type covalency forces yield robust supramolecular bonding even when the presumed classical electrostatic prerequisites for such complexation are profoundly violated. While the computational results presented here focus only on the extremal $\text{RPH}_2\cdots\text{IF}$ versus $\text{RPH}_2\cdots\text{FI}$ limits of this broader picture, the Supplementary Information (SI) includes results for all remaining dihalogen species to illustrate the generality of the resonance-type 3c/4e interaction picture to be sketched below.

Though the conceptual picture we describe is insensitive to many details of the chosen computational method and basis set [55], the inclusion of iodine (for which common Pople-type 6-311++G** basis sets are unavailable) mandates the adoption of a relativistically corrected basis set (e.g., of the pseudopotential LANL2DZ type). For present qualitative purposes, we therefore adopt an unconventional but simple “mixed-PP” basis set of 6-311++G** for all RPH_2 monomers and LANL2DZ for dihalogen monomers of each complex. We employ simple B3LYP density functional methodology throughout this work, but alternative MP2 evaluations at different basis levels were also performed for comparison (see SI). All structures were optimized, and frequencies were computed to confirm equilibrium geometries corresponding to minimum energy points. The binding energy, $\Delta E_{\text{bind}} = E_{(\text{AB})} - E_{(\text{A})} - E_{(\text{B})}$, was calculated as the direct energy difference between optimized dimer and relaxed monomers. All electronic structure calculations were performed with the Gaussian 16 program package [56]. NBO/NRT analyses were performed with NBO 7.0 software [57], and both NBO/NRT analyses and orbital imagery were obtained with the NBOPro@Jmol program [58].

Table 1 summarizes the key structural and binding energy parameters of $\text{RPH}_2\cdots\text{IF}$ and $\text{RPH}_2\cdots\text{FI}$ species as obtained at the adopted “B3LYP/mixed-PP” level, showing the wide range of tuning by various R-substituents. Despite the fact that all complexes are appreciably bound (by circa 3–15 kcal/mol, in defiance of superficial “dipole–dipole” or Coulombic point–charge expectations), interesting structural contrasts are immediately evident between these two classes of species. Focusing first on the orientation angles (Θ) in Table 1, one can see that the $\text{RPH}_2\cdots\text{IF}$ species all maintain nearly linear P \cdots IF alignment ($\Theta_{\text{PIF}} \approx 180^\circ$) and a circa 120° bend angle between RP and IF axes ($\Theta_{\text{RPI}} \approx 120^\circ$).

In contrast, the $\text{RPH}_2\cdots\text{FI}$ species are noticeably tilted away from $\text{P}\cdots\text{FI}$ linearity ($\Theta_{\text{PFI}} \approx 160^\circ$), instead adopting increasingly near-linear alignment with respect to RP and FI axes ($\Theta_{\text{RPF}} \approx 170^\circ$). Such structural tendencies suggest that the principal underlying “linearizing” (H-bond-like) interaction differs in the two cases and that other $\text{RPH}_2\cdots\text{XY}$ dihalogen species of intermediate polarity will likewise exhibit intermediate orientational preferences between these two competing tendencies. Indeed, this is the broader picture obtained from the full set ($X, Y = \text{F, Cl, Br, I}$) of optimized dihalogen structures, with the homopolar $\text{RPH}_2\cdots\text{X}_2$ species forming the approximate “dividing line” between $\text{RPH}_2\cdots\text{IF}$ -like versus $\text{RPH}_2\cdots\text{FI}$ -like structural propensity. These structural features of $\text{RPH}_2\cdots\text{IF}$ -like (“ $\text{P}\cdots\text{IF}$ ”) versus $\text{RPH}_2\cdots\text{FI}$ -like (“ $\text{RP}\cdots\text{F}$ ”) complexes are also consistently exhibited at other theory levels, as shown in SI Tables S1–S3. All such comparisons indicate the adequacy of the adopted B3LYP/mixed-PP model and the extremal $\text{RPH}_2\cdots\text{IF}$ versus $\text{RPH}_2\cdots\text{FI}$ species for describing the full range of $\text{RPH}_2\cdots\text{XY}$ complexation ($X, Y = \text{F, Cl, Br, I}$; $\text{R} = \text{CH}_3, \text{OH}, \text{CF}_3, \text{CN}, \text{NO}_2$), including general consistency with previous MP2/aug-cc-pVTZ-level calculations.

Table 1. Optimized dihalogen $\text{RPH}_2\cdots\text{IF}$ and $\text{RPH}_2\cdots\text{FI}$ complexes (B3LYP/mixed-PP level), showing key structural and energetic descriptors: Bond lengths ($R_{\text{P}\cdots\text{X}}, R_{\text{IF}}, R_{\text{RP}}$; Å) and changes from monomer values ($\Delta R_{\text{IF}}, \Delta R_{\text{RP}}$; Å), orientation angles ($\Theta_{\text{RPX}}, \Theta_{\text{PXY}}$; degrees), dihalogen infrared frequency shift ($\Delta\nu_{\text{IF}}$; cm^{-1}), and binding energy (ΔE_{bind} ; kcal mol^{-1}).

$\text{RPH}_2\cdots\text{IF}$	$R_{\text{P}\cdots\text{I}}$	R_{IF}	ΔR_{IF}	R_{RP}	ΔR_{RP}	Θ_{RPI}	Θ_{PIF}	$\Delta\nu_{\text{IF}}$	ΔE_{bind}
$\text{CH}_3\text{PH}_2\cdots\text{IF}$	2.859	2.071	0.064	1.845	−0.027	115.4	178.2	−84.4	14.60
$\text{OHPH}_2\cdots\text{IF}$	2.854	2.066	0.059	1.652	−0.036	117.1	179.2	−79.6	12.36
$\text{CF}_3\text{PH}_2\cdots\text{IF}$	2.992	2.038	0.031	1.894	−0.002	122.1	177.9	−50.1	7.18
$\text{CNP}_2\cdots\text{IF}$	3.031	2.034	0.027	1.783	−0.014	121.2	177.6	−45.0	5.93
$\text{NO}_2\text{PH}_2\cdots\text{IF}$	3.019	2.031	0.024	1.880	0.000	123.1	175.3	−42.8	5.10
$\text{RPH}_2\cdots\text{FI}$	$R_{\text{P}\cdots\text{F}}$	R_{IF}	ΔR_{IF}	R_{RP}	ΔR_{RP}	Θ_{RPF}	Θ_{PFI}	$\Delta\nu_{\text{IF}}$	ΔE_{bind}
$\text{CH}_3\text{PH}_2\cdots\text{FI}$	2.323	2.114	0.107	1.873	0.001	166.1	164.4	−211.9	3.25
$\text{OHPH}_2\cdots\text{FI}$	2.075	2.197	0.190	1.684	−0.004	164.8	157.4	−320.6	5.85
$\text{CF}_3\text{PH}_2\cdots\text{FI}$	2.624	2.025	0.018	1.900	0.004	172.7	165.1	−52.6	4.43
$\text{CNP}_2\cdots\text{FI}$	2.653	2.020	0.013	1.805	0.008	173.1	164.6	−37.3	4.85
$\text{NO}_2\text{PH}_2\cdots\text{FI}$	2.339	2.055	0.048	1.902	0.022	177.1	160.0	−116.2	6.79

Figure 1 depicts the numerical structural data of Table 1 in graphical form, showing the distinct structural motifs that characterize each extremal “type” of association. Though the graphical imagery primarily allows for the visualization of the angular features of each complex, the progressive shortening of phosphorus–halogen bond length $R_{\text{P}\cdots\text{F}}$ or $R_{\text{P}\cdots\text{I}}$ (as well as concomitant elongation of dihalogen bond length R_{IF}) with increasing binding energy ΔE_{bind} is also discernable in the details of the figure panels. From both Table 1 and Figure 1, one can recognize that the structural effects of different R-substituents are modest compared to that of reversing dihalogen polarity.

Figure 2 presents a graphical display of the trends in tuning binding energy ΔE_{bind} with various R-substituents for the strongly bound complexes of the $\text{RPH}_2\cdots\text{IF}$ type. The graph includes comparison values for the alternative theory levels given in Tables S1–S3 of SI. From Figure 2, one can observe that significant quantitative differences in binding energies are calculated at the various theory levels, but the general trend with respect to the R-substituent variation is reasonably consistent in all cases. A slight exception is seen in the reduced cyano substituent effect in the “unmixed” B3LYP/LANL2DZ, MP2/LANL2DZ theory levels, which may reflect the need for diffuse functions (present in the mixed-PP model but absent in uniform LANL2DZ) to better describe the strong electron-withdrawing effects of this substituent.

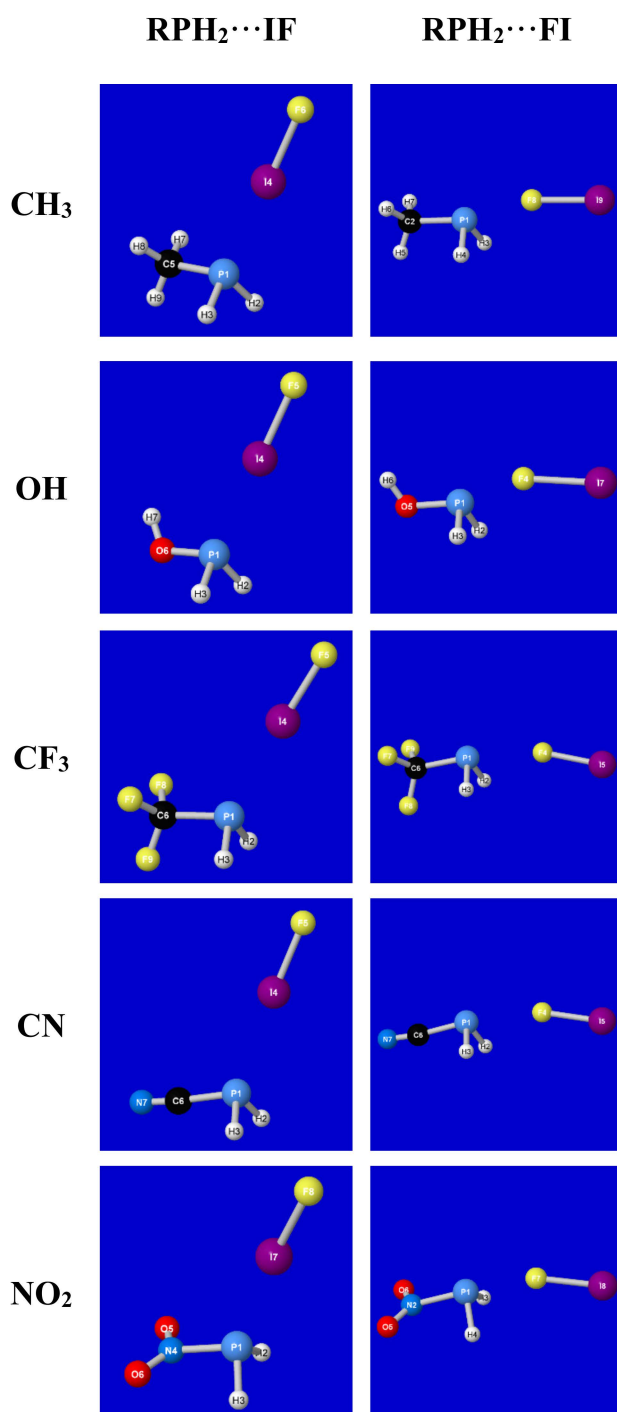


Figure 1. Optimized structures of RPH₂⋯IF and RPH₂⋯FI complexes (cf. Table 1).

Figure 3 shows a corresponding plot of dihalogen frequency shift $\Delta\nu_{\text{IF}}$ with respect to the R-substituent (including comparison results from alternative methods). As shown in the figure, $\Delta\nu_{\text{IF}}$ is strongly red-shifted for the most strongly bound complexes, similar to the well-known spectroscopic signature of H-bonding. Figure 4 exhibits the correlation plot of $\Delta\nu_{\text{IF}}$ (Figure 3) versus ΔE_{bind} (Figure 2) in the RPH₂⋯IF species, showing the high correlation (Pearson $|\chi|^2 = 0.99$) between these experimentally observable quantities that confirms the similarity to H-bonding.

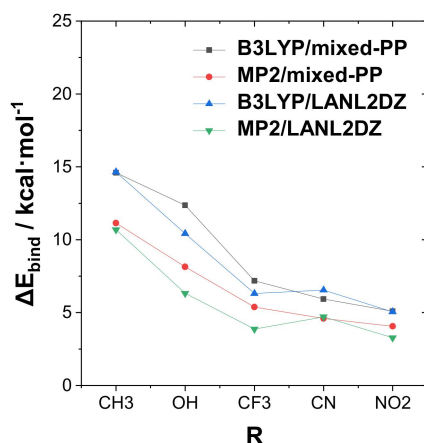


Figure 2. Calculated trend of ΔE_{bind} with substituent R in the $\text{RPH}_2 \cdots \text{IF}$ complexes for four theoretical levels. Note the reversed ordering of the cyano substituent effect on binding energy when diffuse functions are absent (“pure” LANL2DZ; see text).

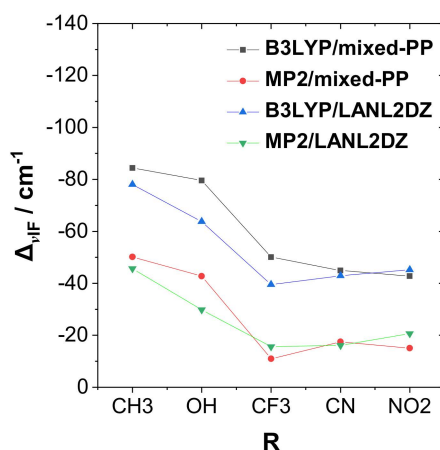


Figure 3. The trend of frequency shift, $\Delta \nu_{\text{IF}}$, with the R-substituent in the $\text{RPH}_2 \cdots \text{IF}$ complexes for four theoretical levels (cf. Figure 2).

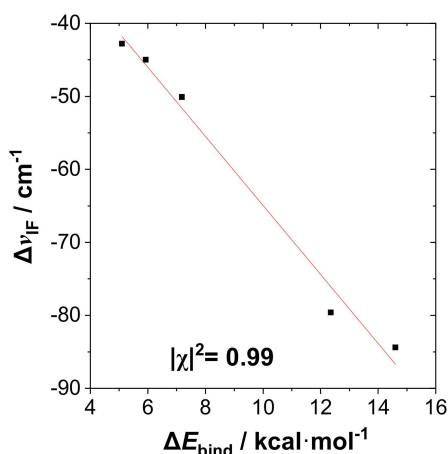


Figure 4. Correlation plot of frequency shift $\Delta \nu_{\text{IF}}$ versus binding energy ΔE_{bind} for the $\text{RPH}_2 \cdots \text{IF}$ species (B3LYP/mixed-PP level), showing the excellent least-squares regression fit (dashed line) and Pearson correlation coefficient ($|\chi|^2 = 0.99$) for these experimentally measurable properties.

Returning to the structural data of Table 1 and Figure 1 for the strongly bound $\text{RPH}_2 \cdots \text{IF}$ complexes, one may note that the intermolecular $\text{P} \cdots \text{I}$ distances vary in the range 2.86–3.03 Å. Table 2 displays

empirical van der Waals (vdW) radii (Pauling values [59]) for the P, I, and F atoms of present interest, showing that the optimized $R_{P\dots I}$ distances in these complexes are all more than 1 Å inside nominal van der Waals contact. This deep penetration into the exponentially repulsive sub-vdW region implies the presence of powerful intermolecular attractive forces (also of exponentially increasing strength) to achieve the net binding energies displayed in Table 1 and Figure 2. In addition, the circa 0.2 Å variation in penetration distance with the R-substituent testifies to the impressive strength of substituent effects that further modulate ΔE_{bind} binding affinity and $R_{P\dots I}$ separation in the deep sub-vdW region.

Table 2. Van der Waals radii of P, I and F atoms (Pauling, Ref. [59]).

Atom	P	I	F	P + I	P + F	I + F
VDW radii/Å	1.9	2.15	1.35	4.0	3.2	3.5

The computed structural and binding characteristics noted above identify the propensities and patterns to be explained and provide helpful clues to the nature of the underlying attractive forces. Even the more weakly bound complexes of the P⋯FI type exhibit optimized P⋯F distances (2.1–2.6 Å) that lie significantly (>0.5 Å) inside vdW contact (circa 3.2 Å, Table 2). Indeed, in both strong RPH₂⋯IF and weak RPH₂⋯FI complexes, the structural features hint at striking resemblances to familiar H-bonding phenomena, including deep sub-vdW penetration (with concomitant covalent bond R_{IF} elongation) and pronounced “linearization” tendency (albeit along different 3-center axes: P⋯IF in the RPH₂⋯IF case versus RP⋯F in the RPH₂⋯FI case). We take up NBO/NRT investigation of these apparent similarities and bonding relationships in the following sections.

3. NBO/NRT Descriptors

As suggested in (1a,b) above, an NBO/NRT analysis of B⋯HA hydrogen-bonding phenomena reveals a host of characteristic correlations [22,23,60] that implicate resonance-type $n_{\text{B}} \rightarrow \sigma_{\text{AH}}^*$ “charge transfer” interactions as the fundamental electronic origin of H-bonding, consistent with the earliest results of NBO analysis [61–63]. This conclusion also supports a considerable variety of other experimental and theoretical evidence [64–68] for the charge–transfer nature of H-bonding. The question here is whether similar NBO/NRT diagnostics may provide analogous associations with $n \rightarrow \sigma^*$ (lone pair to valence antibond) donor–acceptor interactions of the present species.

The analogies of the preceding section suggest appropriate NBO/NRT descriptors for the corresponding ⋯X— (“X-ogen”) species that can be similarly visualized in simple orbital overlap terms. For RPH₂⋯IF complexes, the key feature of envisioned P⋯I—F “halogen bonding” is the donor–acceptor delocalization of electronic charge from an occupied donor NBO of P (lone pair n_{P}) to the favorably polarized acceptor NBO (antibond σ_{IF}^*) of the P⋯I—F triad. For RPH₂⋯FI complexes, where the $n_{\text{P}}-\sigma_{\text{IF}}^*$ overlap is unfavorable, the analogous feature of envisioned F⋯P—R “pnictogen bonding” is the donation from a fluorine lone pair (n_{F}) to the proximal antibond (σ_{PR}^*) of the phosphine monomer. Each such $n \rightarrow \sigma^*$ delocalization can be alternatively quantified in terms of energetic (perturbative $\Delta E^{(2)}_{n\sigma^*}$ or variational deletion $\Delta E^{(\text{\$DEL})}_{n\sigma^*}$), charge transfer ($Q_{n\sigma^*}$), or fractional NRT bond order ($b_{\text{P}\dots\text{I}}$ or $b_{\text{P}\dots\text{F}}$) descriptors.

3.1. Energy Descriptors

Table 3 summarizes estimates of the $\Delta E_{n\sigma^*}$ stabilization energy associated with each type of delocalization in the strongly bound RPH₂⋯IF species. The first two columns display 2nd-order perturbative $\Delta E^{(2)}_{n\sigma^*}$ estimates for $n_{\text{P}} \rightarrow \sigma_{\text{IF}}^*$ (“halogen bond”) and $n_{\text{I}} \rightarrow \sigma_{\text{PR}}^*$ (“pnictogen bond”) contributions. The final two columns of Table 3 display corresponding $\Delta E^{(\text{\$DEL})}_{n\sigma^*}$ variational deletion estimates, obtained as the variational energy raising when the specific $n \rightarrow \sigma^*$ NBO interaction is deleted from the total energy evaluation. The two estimates are seen to be in reasonable qualitative agreement for each interaction type. The $\Delta E^{(2)}_{n(\text{P}) \rightarrow \sigma^*(\text{IF})}$ values range from 19 to 37 kcal/mol (in the same order as

ΔE_{bind}), whereas $\Delta E^{(2)}_{n(\text{I}) \rightarrow \sigma^*(\text{FI})}$ is relatively negligible in each case, and a similar pattern is seen in the $\Delta E^{(\text{SDEL})}_{n\sigma^*}$ values. We therefore expect that the stabilization energy of the $n_{\text{P}} \rightarrow \sigma^*_{\text{IF}}$ interaction is the dominant attractive contribution to the structure and binding of $\text{RPH}_2 \cdots \text{IF}$ complexes, similar to the dominance of the $n_{\text{B}} \rightarrow \sigma^*_{\text{AH}}$ interaction in H-bonding.

Table 3. $\Delta E_{n\sigma^*}$ stabilization energy estimates(kcal/mol) for halogen-type [$n(\text{P}) \rightarrow \sigma^*(\text{IF})$] and leading pnico-gen-type [$n(\text{I}) \rightarrow \sigma^*(\text{PR})$] interactions of $\text{RPH}_2 \cdots \text{IF}$ complexes, showing perturbative $\Delta E^{(2)}_{n\sigma^*}$ values in the first two columns and variational deletion $\Delta E^{(\text{SDEL})}_{n\sigma^*}$ values in the final two columns (The connected R-atom of each σ^*_{PR} acceptor NBO is shown underlined in the species listing.).

Species	$\Delta E^{(2)}_{n(\text{P}) \rightarrow \sigma^*(\text{IF})}$	$\Delta E^{(2)}_{n(\text{I}) \rightarrow \sigma^*(\text{PR})}$	$\Delta E^{(\text{SDEL})}_{n(\text{P}) \rightarrow \sigma^*(\text{IF})}$	$\Delta E^{(\text{SDEL})}_{n(\text{I}) \rightarrow \sigma^*(\text{PR})}$
<u>C</u> $\text{H}_3\text{PH}_2 \cdots \text{IF}$	36.96	1.32	51.87	1.47
<u>O</u> $\text{HPH}_2 \cdots \text{IF}$	35.99	2.12	51.88	2.60
<u>C</u> $\text{F}_3\text{PH}_2 \cdots \text{IF}$	22.42	1.62	28.56	1.69
<u>C</u> $\text{NPH}_2 \cdots \text{IF}$	20.73	1.40	24.80	1.73
<u>N</u> $\text{O}_2\text{PH}_2 \cdots \text{IF}$	19.12	2.69	23.73	2.64

For the weakly bound $\text{RPH}_2 \cdots \text{FI}$ species, the situation is more complex. Due to the unfavorable polarization of σ^*_{FI} away from the n_{P} lone pair, the single $n_{\text{P}} \rightarrow \sigma^*_{\text{IF}}$ interaction that dominates bonding in $\text{RPH}_2 \cdots \text{IF}$ species becomes only one of several such competing contributions to net binding. Specifically, for the opposed $\text{F} \cdots \text{P} \text{---} \text{R}$ (pnico-gen bonding) motif, three possible n_{F} lone pairs (one of sigma type and two of pi type) and three σ^*_{PY} acceptors (one σ^*_{PR} and two σ^*_{PH}) are within proximal interaction range as potential contributors to a complex resonance mixture. A particular interaction such as $n_{\text{F}}^{(\sigma)} \rightarrow \sigma^*_{\text{PR}}$ therefore represents only one of the nine related $n \rightarrow \sigma^*$ interactions that may exert leverage on angular structure and binding energy. In such a case, only a more nuanced resonance-type description (see the discussion of NRT bond orders below) can describe the complete bonding picture that provides useful correlations with experimentally measurable properties. We therefore defer further discussion of $\text{RPH}_2 \cdots \text{FI}$ complexes to a later subsection.

3.2. Graphical Orbital Overlap Imagery

A powerful aspect of NBO energetic descriptors is their intimate relationship to the intuitive visual imagery of the orbital overlap, the NBO counterpart of the well-known “Mulliken approximation” [69–72] that underlies semi-empirical MO theory. For such visualization purposes, “pre-orthogonal” NBOs (PNBOs) [49] are employed that maintain free-space symmetries (cartoon-like “textbook” shapes) of non-interacting NBOs prior to the actual distortions of the molecular environment. Table 4 displays such PNBO visualizations for the various donor–acceptor $n \rightarrow \sigma^*$ interactions of halogen ($n_{\text{P}} \rightarrow \sigma^*_{\text{IF}}$; first column) or pnico-gen ($n_{\text{I}}^{(\pi)} \rightarrow \sigma^*_{\text{PR}}$, $n_{\text{I}}^{(\sigma)} \rightarrow \sigma^*_{\text{PR}}$; final two columns) types, with corresponding numerical $\Delta E^{(2)}_{n\sigma^*}$ values (Table 3) inset in the panels.

For example, in the three panels for $\text{CH}_3\text{PH}_2 \cdots \text{IF}$ (first row of Table 4) one can see that the “end-on” (sigma-type) overlap of σ^*_{IF} with the nitrogen lone pair n_{P} (left panel) is much stronger than the “edge-on” (pi-type) overlap of σ^*_{PR} with the in-plane iodine $n_{\text{I}}^{(\pi)}$ (middle panel) or $n_{\text{I}}^{(\sigma)}$ (right panel) lone pairs, in accordance with the $\Delta E^{(2)}_{n\sigma^*}$ values shown in each panel. Even a casual glance at the overall patterns of the orbital overlap in Table 4 can therefore make clear why the slight variations of orbital shape with R-substitution do not materially alter the strong propensity for halogen-type ($n_{\text{P}} \rightarrow \sigma^*_{\text{IF}}$) rather than pnico-gen-type ($n_{\text{I}}^{(\pi)} \rightarrow \sigma^*_{\text{PR}}$, $n_{\text{I}}^{(\sigma)} \rightarrow \sigma^*_{\text{PR}}$) bonding throughout the $\text{RPH}_2 \cdots \text{IF}$ series, as numerically displayed in Table 3.

Though the donor–acceptor $\Delta E_{n\sigma^*}$ stabilization energies of Table 3 display a qualitative ordering pattern similar to that of the ΔE_{bind} binding energies of Table 1, it is evident that these estimates significantly “overshoot” the final net binding energy. This is to be expected, because each stabilizing donor–acceptor interaction is opposed by steric repulsions of the corresponding $\Delta E_{n\sigma}$ donor–donor interaction. Table 5 displays orbital overlap diagrams and inset values of the pairwise estimates $\Delta E^{(\text{PW})}$

$n-\sigma$ for repulsive “steric exchange energy” [54] between occupied NBOs of the $RPH_2\cdots IF$ series. As shown in the panels, the two leading intermolecular repulsions refer to the n_P-n_I steric clash between lone pairs of proximal P and I atoms (left) and $n_P-\sigma_{IF}$ clash between a lone pair and bond of the halogen bond $P\cdots I-F$ triad. However, weaker $n_I-\sigma_{PR}$, $n_I-\sigma_{PH}$ clashes of the alternative pnictogen bond triads ($I\cdots P-R$, $I\cdots P-H$) also contribute to sub-vdW steric opposition, thereby further offsetting the apparently “excessive” NBO estimate of donor–acceptor attraction needed to achieve the final equilibrium geometry and net binding energy.

Table 4. “Pre-orthogonal” natural bond orbital (PNBO) orbital overlap diagrams (with perturbative $\Delta E^{(2)}_{n\sigma^*}$ stabilization energy (kcal/mol) as inset) for $RPH_2\cdots IF$ complexes (cf. Table 3), showing the usefulness of Mulliken-type orbital overlap visualizations in “guesstimating” donor–acceptor interaction strengths.

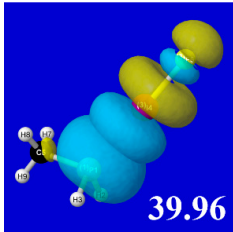
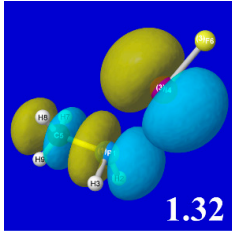
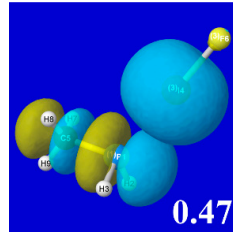
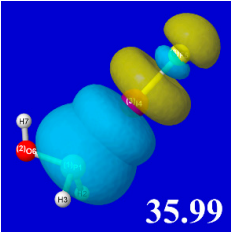
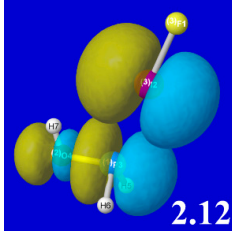
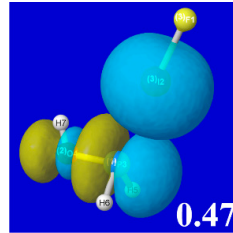
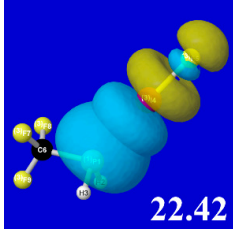
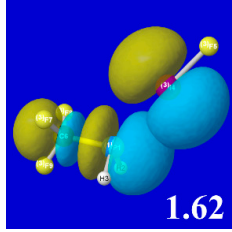
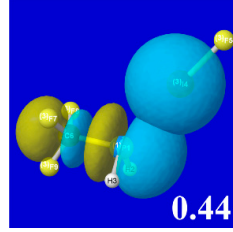
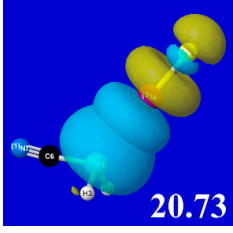
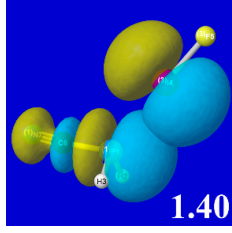
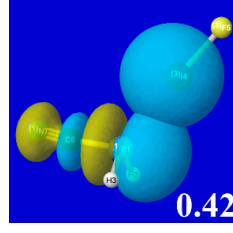
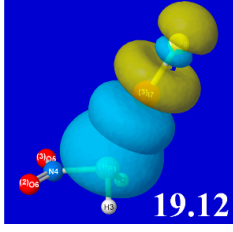
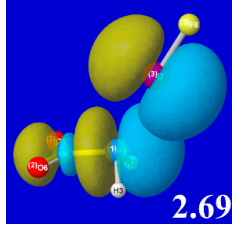
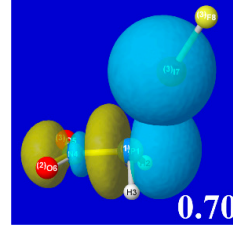
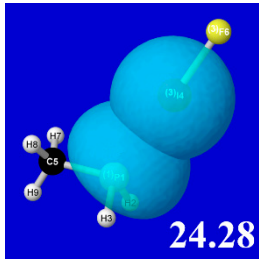
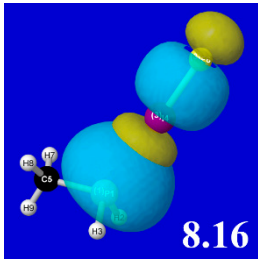
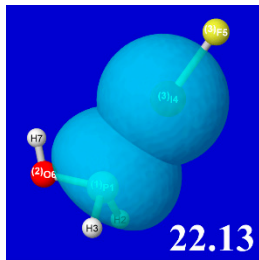
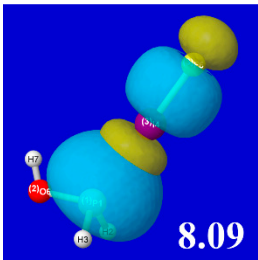
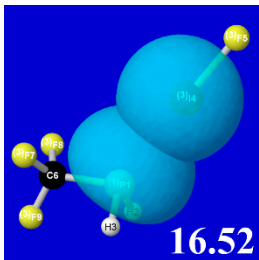
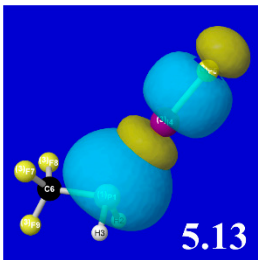
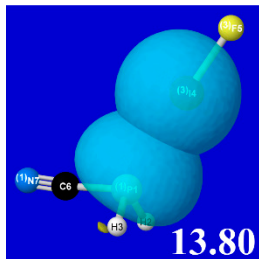
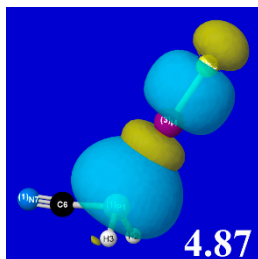
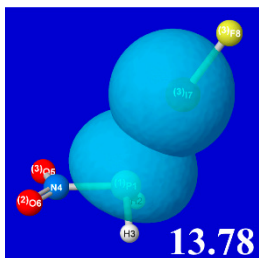
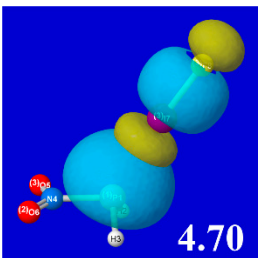
Species	$n_P \rightarrow \sigma^*_{IF}$	$n_I(\pi) \rightarrow \sigma^*_{PR}$	$n_I(\sigma) \rightarrow \sigma^*_{PR}$
$\underline{CH}_3PH_2\cdots IF$	 39.96	 1.32	 0.47
$\underline{OHPH}_2\cdots IF$	 35.99	 2.12	 0.47
$\underline{CF}_3PH_2\cdots IF$	 22.42	 1.62	 0.44
$\underline{CNPH}_2\cdots IF$	 20.73	 1.40	 0.42
$\underline{NO}_2PH_2\cdots IF$	 19.12	 2.69	 0.70

Table 5. $\Delta E^{(PW)}$ _{donor-donor} repulsion energy estimates (kcal/mol) for leading n_P - n_I and n_P - σ_{IF} steric clashes of RPH₂...IF complexes, obtained from steric-keyword analysis.

Species	$\Delta E^{(PW)}$ _{n(P)-n(I)}	$\Delta E^{(PW)}$ _{n(P)-\sigma(IF)}
<u>CH</u> ₃ PH ₂ ...IF	 24.28	 8.16
<u>OH</u> PH ₂ ...IF	 22.13	 8.09
<u>CF</u> ₃ PH ₂ ...IF	 16.52	 5.13
<u>CN</u> PH ₂ ...IF	 13.80	 4.87
<u>NO</u> ₂ PH ₂ ...IF	 13.78	 4.70

PNBO visualizations for occupied n_P , n_I , and σ_{IF} NBOs (not shown) similarly serve to rationalize the trends in repulsive donor-donor interactions (Table 5). Furthermore, it becomes evident from graphical comparisons that all such orbital visualizations for the presently considered species are highly analogous to those for the corresponding interactions of H-bonding [22], which is in accordance with the patterns and relationships inferred from numerical descriptors.

3.3. Structural, Energetic, and Spectroscopic Effects of Donor–Acceptor Deletion

Still another widget from the NBO toolbox can be used to exhibit the profound effects of $n_P \rightarrow \sigma^*_{IF}$ delocalization on supramolecular bonding properties. Similar to the variational \$DEL-deletion $\Delta E^{(\$DEL)}_{n(P) \rightarrow \sigma^*(IF)}$ evaluations of $n \rightarrow \sigma^*$ donor–acceptor strength in the equilibrium species (Table 3), one can variationally reoptimize the structure for the associated $E^{(\$DEL)}_{n(P) \rightarrow \sigma^*(IF)}$ potential energy surface in which $n \rightarrow \sigma^*$ delocalization is absent, as though nature (in accordance with common textbook presentations) failed to include such interactions.

Table 6 displays results for the variational reoptimization of a simple 2D model of $RPH_2 \cdots IF$ dissociation, with the $n_P \rightarrow \sigma^*_{IF}$ interaction deleted. Starting from the equilibrium values of the actual $RPH_2 \cdots IF$ species, the distance variables $R_{P \cdots I}$, R_{IF} (for fixed idealized angular geometry) were optimized to find the new binding energy (ΔE_{bind}) and shifts ($\Delta R_{P \cdots I}$, ΔR_{IF} , $\Delta \Delta E_{bind}$) that describe the hypothetical “resonance-free” $RPH_2 \cdots IF$ that lacks $n_P \rightarrow \sigma^*_{IF}$ donor–acceptor attraction. From the resulting values, one sees that characteristic structural and energetic signatures of $RPH_2 \cdots IF$ bonding are lost when the $n_P \rightarrow \sigma^*_{IF}$ interaction is “turned off;” the RPH_2 and IF monomers retreat (by circa 1.3 Å) to beyond-vdW separation, the characteristic R_{IF} elongation (associated with vibrational red-shifting) from isolated monomer geometry essentially disappears, and the net binding energy drops precipitously (by >80%) to a remnant value that might plausibly be associated with residual “dipole–dipole” forces. Note that the monomer dipole moments or other aspects of electron density distribution are scarcely altered in the \$DEL-reoptimized geometry, and the “lost” energy of $n_P \rightarrow \sigma^*_{IF}$ stabilization is negligibly small (1.59 kcal/mol) at the reoptimized separation distance. From the results of such \$DEL-deletion calculations, one recognizes $n_P \rightarrow \sigma^*_{IF}$ stabilization to be the unique “smoking gun” that is both necessary and sufficient to bring the supramolecular complex to the actual short-range geometry and other signatures of halogen bonding, which is in direct correspondence to the analogous $n_B \rightarrow \sigma^*_{HA}$ role in H-bonding.

Table 6. Relaxed geometrical parameters ($R_{P \cdots I}$, R_{IF} ; Å), binding energy (ΔE_{bind} ; kcal/mol), and dihalogen stretching frequency (ν_{IF} ; cm^{-1}) (with associated shifts from true equilibrium structure in parentheses) for \$DEL-type variational reoptimizations, with the $n_P \rightarrow \sigma^*_{IF}$ charge–transfer interaction deleted.

Species	$R_{P \cdots I}$ ($\Delta R_{P \cdots I}$)	R_{IF} (ΔR_{IF})	ΔE_{bind} ($\Delta \Delta E_{bind}$)
$CH_3PH_2 \cdots IF$	4.20 (1.34)	2.007 (−0.064)	2.32 (−12.28)
$OHPH_2 \cdots IF$	4.29 (1.43)	2.006 (−0.060)	1.31 (−11.05)
$CF_3PH_2 \cdots IF$	4.34 (1.35)	2.003 (−0.035)	0.96 (−6.22)
$CNPH_2 \cdots IF$	4.37 (1.34)	2.003 (−0.031)	0.63 (−5.30)
$NO_2PH_2 \cdots IF$	4.40 (1.39)	2.003 (−0.028)	0.38 (−4.72)

Still another use of \$DEL-deletion techniques is to prepare relaxed-scan potential curves that illustrate how intermolecular $n \rightarrow \sigma^*$ interactions lead to net binding against the essentially repulsive potential curve for hypothetical monomers that interact without benefit of resonance-type stabilization. Figure 5 illustrates such potential curves for $CH_3PH_2 \cdots IF$ dissociation, showing the potential curve for the fully interacting monomers (squares, black line, “ ΔE_{bind} ”; cf. Table 1) versus that for “resonance-free” monomers that lack intermolecular $n \rightarrow \sigma^*$ interactions (triangles, blue line, repulsive “ ΔE_r ”). The “missing” resonance-type (purely attractive) interactions are shown as the difference curve (diamonds, red line, attractive “ ΔE_a ”). The blue curve exhibits a feeble attractive well beyond vdW contact at $R_{P \cdots I} \approx 4.0 \text{ Å}$ (presumably due to “dipole–dipole” attraction) but rises steeply as a repulsive steric wall in the sub-vdW region. Already in the region of the initial sub-vdW penetration, the red curve ($n \rightarrow \sigma^*$ resonance attraction) has achieved sufficient stabilization to oppose thermal fluctuations ($kT \approx 0.6 \text{ kcal/mol}$ at 300K) and yield significant sub-vdW binding in the black (full potential) curve down to $R_{P \cdots I} \approx 2.9$ equilibrium separation. Inside this equilibrium distance, the intermolecular

n - σ steric repulsion overcomes n - σ^* attraction to give the steeply repulsive inner wall of the full potential, resonance-shifted inside circa 2.5 Å. Where such n_P - σ_{IF} versus n_P - σ^*_{IF} “cross-over” occurs will evidently depend on the polarization of the dihalogen bond and is therefore expected to shift to a progressively larger $R_{P\dots I}$ separation (and weakened ΔE_{bind}) for other members of the dihalogen series, thereby appearing as a secondary “electrostatic” modulating effect on the overall halogen bonding phenomenon.

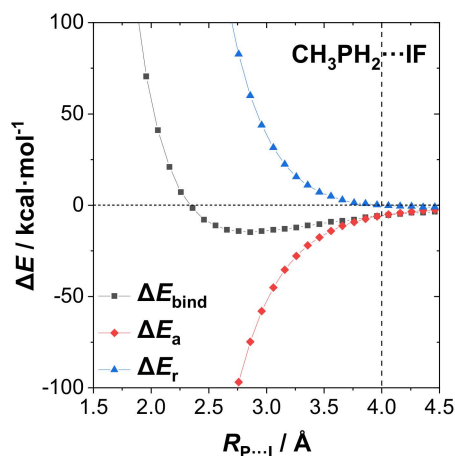


Figure 5. Potential curves for $\text{CH}_3\text{PH}_2\dots\text{IF}$ dissociation (B3LYP/mixed-PP level), showing (i) repulsive “resonance-free” potential ΔE_r (blue, triangles) with all resonance-type intermolecular delocalizations deleted, (ii) the stabilizing potential for attractive resonance-type interactions ΔE_a (red, diamonds) that were deleted in the resonance-free model, and (iii) the combined “full” potential ΔE_{bind} (sum of (i), (ii)) (black, squares).

3.4. Charge and Polarity Descriptors

Table 7 displays various NBO charge/polarization descriptors for the $\text{RPH}_2\dots\text{IF}$ species (net intermolecular charge transfer Q_{CT} , atomic charges q_P , q_I , and q_F of the $\text{P}\dots\text{I}\text{—F}$ triad, IF bond ionicity i_{IF} [73]), compared with those for isolated IF monomer. As shown for the dihalogen monomer in the final column of the table, I–F bond ionicity ($-1 \leq i_{\text{IF}} \leq +1$, related to dipole moment direction from I to F) tends to increase steadily with strength of $\text{RPH}_2\dots\text{IF}$ binding or net Q_{CT} . This trend reflects the expected dominance of the $n_P \rightarrow \sigma^*_{\text{IF}}$ interaction, which is evidently enhanced (cf. overlap diagrams of Table 5) if σ_{IF} bond ionicity increases toward F, thereby polarizing the σ^*_{IF} antibond toward I (and adjacent n_P). The combined effect of repolarization (i_{IF}) and net charge transfer (Q_{CT}) is to give a somewhat irregular pattern to individual atomic charges q_I , q_F , but all such IF charge descriptors are seen to properly “add up,” as they must according to the strict logic of a natural population analysis.

Table 7. Total $\text{RPH}_2 \rightarrow \text{IF}$ charge transfer (Q_{CT} ; e), atomic charges (q_P , q_I , q_F), and σ_{IF} bond ionicity (i_{IF}) in $\text{RPH}_2\dots\text{IF}$ complexes, compared with isolated IF monomer.

Species	Q_{CT}	q_P	q_I	q_F	i_{IF}
$\text{CH}_3\text{PH}_2\dots\text{IF}$	0.2405	0.4084	0.3227	−0.5632	0.496
$\text{OHPH}_2\dots\text{IF}$	0.2432	0.7345	0.3144	−0.5576	0.486
$\text{CF}_3\text{PH}_2\dots\text{IF}$	0.1413	0.2974	0.3857	−0.5270	0.485
$\text{CNP}_2\dots\text{IF}$	0.1255	0.3493	0.3924	−0.5179	0.480
$\text{NO}_2\text{PH}_2\dots\text{IF}$	0.1137	0.4496	0.4013	−0.5150	0.478
IF	-	-	0.4691	−0.4691	0.469

In the RPH₂ monomer, the phosphorus charge q_P reflects the still more complex effects of sigma-type induction versus intra- and intermolecular lone pair delocalizations. One can see in the table the evident effect of bonding the phosphorus to more electronegative oxygen ($q_P \approx 0.73$) or nitrogen ($q_P \approx 0.45$) rather than carbon ($q_P \approx 0.3$ – 0.4). However, also important in the present context is the intra- versus intermolecular competition for charge donation from the “busy” phosphorus lone pair n_P to various pi-type acceptor orbitals of the R-substituent (e.g., π_{CN} , π_{NO}) versus the intermolecular $n_P \rightarrow \sigma^*_{IF}$ interaction of principal interest.

3.5. NRT Bond Order Descriptors

Perhaps the most useful and general descriptors of supramolecular bonding are NRT bond orders $\{b_{AB}\}$, which balance the nuances of multiple resonance structure contributions to give a single composite measure of A...B “connectivity.” As described elsewhere [40–43], NRT bond orders differ from those of the Pauling type, particularly in their close association with the first-order reduced density matrix [74] (rather than assumed valence bond (VB) wavefunction) of the system. A vastly improved convex solver [75] for the NRT variational objective function is a leading feature of the NBO 7.0 program [57].

The first three columns of Table 8 show calculated NRT bond orders for the key P/I/F atoms in both the RPH₂...IF and RPH₂...FI series. The values vary rather continuously over the range $0 \leq b_{AB} \leq 1$, with no apparent “dividing line” between what should be described as the “covalent bond” (stick) versus the “noncovalent interaction” (dots). Most surprising in these species are the non-vanishing bond orders for the “long-bond” [76–78] interactions of P...F (in P...I—F triads) or P...I type (in P...F—I triads). Though negligibly small in the most strongly bound RPH₂...IF species, certain P...I long bonds achieve bond orders that rival or exceed those of familiar $b_{P...F}$ or b_{IF} linkages (e.g., in OHPH₂...FI).

Table 8. Natural resonance theory (NRT) bond orders and bond order sums for the $b_{P...I}$ halogen bond, b_{IF} covalent bond, and $b_{P...F}$ long bond of RPH₂...IF complexes (P...IF triad; upper rows) or the $b_{P...F}$ pnictogen bond, b_{IF} covalent bond, and $b_{P...I}$ long bond of RPH₂...FI complexes (F...PI triad; lower rows). Note the near-constant “bond conservation” of the summed bond orders within each 3c/4e triad (final column).

Species	$b_{P...I}$	b_{IF}	$b_{P...F}$	$b_{P...I} + b_{IF}$	$b_{P...I} + b_{IF} + b_{P...F}$
CH ₃ PH ₂ ...IF	0.47	0.60	0.00	1.07	1.07
OHPH ₂ ...IF	0.45	0.59	0.00	1.04	1.04
CF ₃ PH ₂ ...IF	0.31	0.64	0.11	0.95	1.05
CNPH ₂ ...IF	0.28	0.67	0.10	0.94	1.04
NO ₂ PH ₂ ...IF	0.32	0.67	0.10	0.99	1.09
Species	$b_{P...F}$	b_{IF}	$b_{P...I}$	$b_{P...F} + b_{IF}$	$b_{P...F} + b_{IF} + b_{P...I}$
CH ₃ PH ₂ ...FI	0.20	0.59	0.27	0.80	1.06
OHPH ₂ ...FI	0.34	0.45	0.36	0.79	1.14
CF ₃ PH ₂ ...FI	0.09	0.89	0.07	0.98	1.05
CNPH ₂ ...FI	0.08	0.92	0.05	1.00	1.05
NO ₂ PH ₂ ...FI	0.16	0.80	0.12	0.96	1.07

The final two columns of Table 8 show two-term or three-term bond order sums that test the validity of resonance-type “bond order conservation” [48] rules (cf. (1a,b) for H-bonding). The two-term sum (column 4) exhibits significant deviations from the expected unit value in a simple two-resonance model for a mono-valent central atom of the 3c/4e triad. These deviations indicate the need for a three-term sum (three-resonance model) that includes long-bond contributions (column 5). Remaining deviations from unity in the three-term sums of column 5 indicate additional conjugative or

hyperconjugative interactions with the R-substituent that require still higher-order resonance couplings. All these results suggest the close relationship of NRT bond orders to the familiar resonance-theoretic concepts of the organic chemist, as well as their usefulness in expected empirical correlations with experimentally measurable structural, energetic, and spectroscopic properties, as discussed in the following section.

4. Mutual Correlations of NBO/NRT Descriptors with Measurable Properties

The principal NBO descriptors of donor–acceptor interactions (such as $\Delta E^{(2)}_{n\sigma^*}$, $\Delta E^{(\$DEL)}_{n\sigma^*}$, $Q_{n\sigma^*}$, ...) intrinsically focus on orbitals of a specific $n \rightarrow \sigma^*$ “delocalization” from a specific Lewis structural bonding pattern. Such orbital-specific descriptors are valuable when a single “parent” Lewis structure and “child” $n \rightarrow \sigma^*$ delocalization clearly dominate quantum mechanical descriptions of the structural, energetic, and spectroscopic properties of the chosen system. However, for many chemical systems of interest (including the $RPH_2 \cdots FI$ species considered here), multiple $n \rightarrow \sigma^*$ interactions come into play, corresponding to contributions of alternative resonance–structural bonding patterns that may no longer be “child-like” compared to a reference parent pattern. Such cases demand the more nuanced NRT descriptors such as interatomic bond orders $\{b_{AB}\}$ that balance the many possible orbital interactions contributing to the overall resonance hybrid.

As could be anticipated from the empirical origins of bond order descriptors in the pre-quantum mechanical conceptions of “mesomerism” theory [43], the “averaged” (fractional) character of NRT bond orders $\{b_{AB}\}$ and their association with atoms (rather than orbitals) makes them better adapted to describe empirical correlations with measurable properties. Well-known examples include bond order–bond length (b_{AB} – R_{AB}) [79], bond order–bond energy [80], and bond order–bond frequency (Badger’s rule) [81] relationships. Here we wish to briefly examine the mutual correlations of NBO/NRT descriptors in the single strong $n \rightarrow \sigma^*$ limit (where orbital-type descriptors may suffice) as well as the more general correlations of NRT bond orders with experimentally measurable properties, spanning the full set of $RPH_2 \cdots IF/FI$ species considered in this work.

Starting with the $RPH_2 \cdots IF$ series, in which the $n_P \rightarrow \sigma^*_{IF}$ interaction plays a clearly dominant role, we first consider the mutual correlations of $\Delta E^{(2)}_{n\sigma^*}$, $\Delta E^{(\$DEL)}_{n\sigma^*}$, $Q_{n\sigma^*}$, $b_{P \cdots I}$ descriptors for this interaction. Taking perturbative $\Delta E^{(2)}_{n\sigma^*}$ as the base descriptor for the group, we display (a) $\Delta E^{(2)}_{n\sigma^*}$ – $\Delta E^{(\$DEL)}_{n\sigma^*}$, (b) $\Delta E^{(2)}_{n\sigma^*}$ – $Q_{n\sigma^*}$, and (c) $\Delta E^{(2)}_{n\sigma^*}$ – $b_{P \cdots I}$ correlation diagrams in successive panels (a)–(c) of Figure 6. The displayed least-squares regression lines and Pearson $|\chi|^2$ correlation coefficients demonstrate the high quality of these mutual correlations: In the range 0.94–0.99 for NBO-specific descriptors, but slightly lower (0.94) for correlation with the NRT bond order $b_{P \cdots I}$ (presumably due to the proper inclusion of secondary donor–acceptor interactions with R-substituents that are present only in the latter). The results show that descriptors of this group could be chosen rather interchangeably for correlations with measurable experimental properties when a single donor–acceptor interaction such as $n_P \rightarrow \sigma^*_{IF}$ is clearly dominant.

For more general correlations with measurable experimental properties such as (a) intermolecular $R_{P \cdots I}$ or $R_{P \cdots F}$, (b) intramolecular R_{IF} , (c) binding energy ΔE_{bind} , or (d) infrared stretching frequency ν_{IF} , we employed the NRT bond order b_{AB} (of specified atoms A, B) as base descriptor in the correlation diagrams of Figure 7a–d, extending the correlations to both $RPH_2 \cdots IF$ (black; approximate two-resonance) and $RPH_2 \cdots FI$ (red: Multi-resonance) series. As examples of bond order–bond length correlations, Figure 7a displays the intermolecular $b_{P \cdots X}$ – $R_{P \cdots X}$ correlations ($X = I, F$) for each series, with reasonably high correlations ($|\chi|^2 = 0.92$) in each case. Figure 7b similarly displays the intramolecular b_{IF} – R_{IF} correlation for the dihalogen monomer, with still higher correlation coefficients ($|\chi|^2 = 0.94$ for $RPH_2 \cdots IF$, $|\chi|^2 = 0.98$ for $RPH_2 \cdots FI$ species). As examples of bond order–bond energy correlation, Figure 7c displays the $b_{P \cdots X}$ – ΔE_{bind} correlations ($X = I, F$), with similar correlation coefficients ($|\chi|^2 = 0.94$) in each series. Finally, as bond order–bond frequency examples, Figure 7d displays the b_{IF} – $\Delta \nu_{IF}$ correlations, again with high correlation coefficients ($|\chi|^2 = 0.95$ for $RPH_2 \cdots IF$, $|\chi|^2 = 0.98$ for $RPH_2 \cdots FI$ species). All these correlations suggest the high predictive utility of NRT bond orders for both the

tuning effects of R-substituents and the polarity variations of the various dihalogen monomers that govern the broad range of binding energies in these supramolecular species.

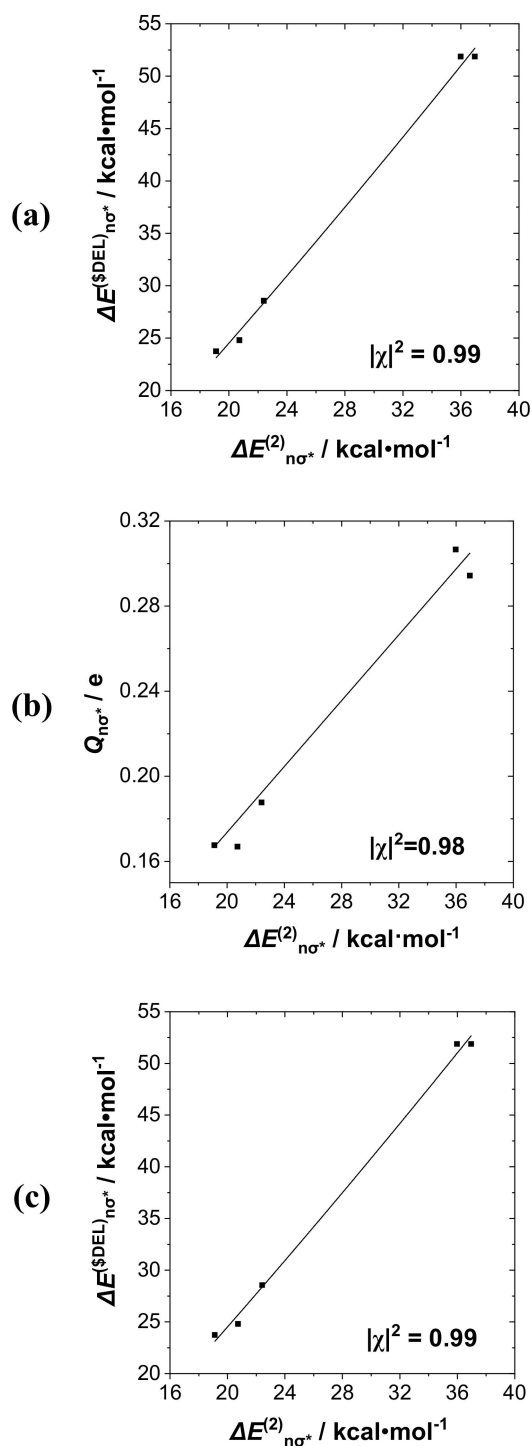


Figure 6. Correlation diagrams for (a) $\Delta E^{(2)}_{n\sigma^*}$ - $\Delta E^{(\$DEL)}_{n\sigma^*}$, (b) $\Delta E^{(2)}_{n\sigma^*}$ - $Q_{n\sigma^*}$, and (c) $\Delta E^{(2)}_{n\sigma^*}$ - $b_{P...I}$ descriptors of $\text{RPH}_2\cdots\text{IF}$ species, showing least-squares regression line and Pearson correlation coefficient $|\chi|^2$ for each pairing.

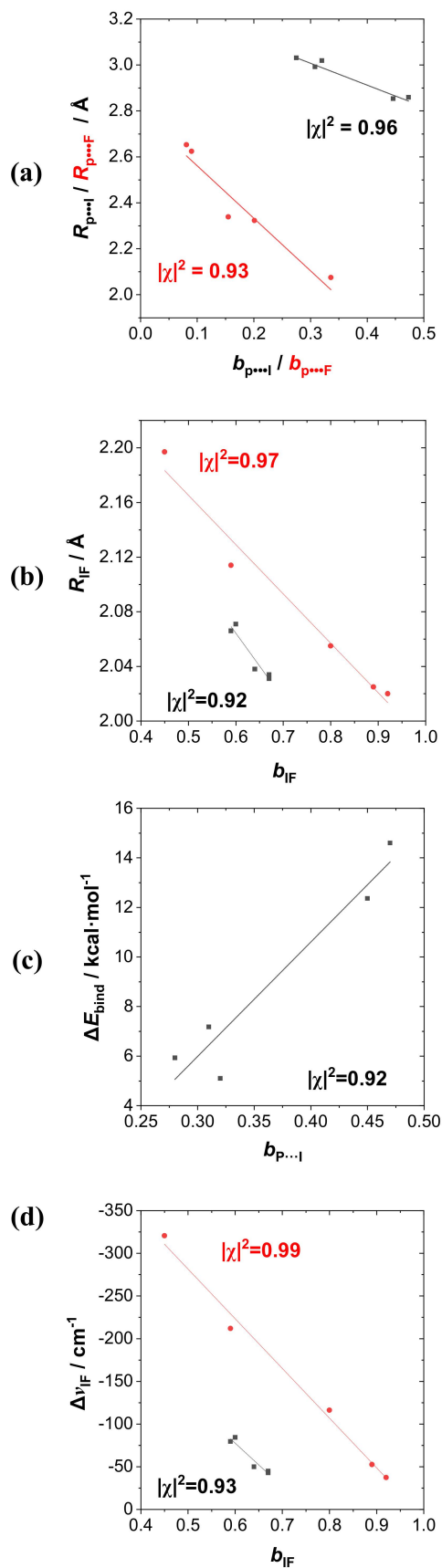


Figure 7. Bond order–bond property correlation diagrams for (a) $b_{p...I}$ – $R_{p...I}$, (b) b_{IF} – R_{IF} , (c) $b_{p...I}$ – ΔE_{bind} , and (d) b_{IF} – $\Delta\nu_{IF}$ descriptors of RPH₂...IF (black) and RPH₂...FI (red) species, showing least-squares regression line and Pearson correlation coefficient $|\chi|^2$ for each pairing.

5. Summary and Conclusions

We have computationally investigated the nature of supramolecular bonding in a series of R-substituted phosphine...dihalogen complexes (RPH₂...IF/Fl, R = CH₃, OH, CF₃, CN, NO₂), focusing on the electronic origin of what might be identified as a “halogen bond,” “pnictogen bond,” or some combination of both. For this purpose, we employed a broad variety of natural bond orbital (NBO) and natural resonance theory (NRT) descriptors, searching for relationships to hydrogen bonding or other known forms of intermolecular attraction (often loosely termed “noncovalent”).

Our results show that resonance-type “ $n \rightarrow \sigma^*$ ” delocalization (leading to fractional intermolecular bond orders) is the dominant feature of halogen-type (e.g., $n_P \rightarrow \sigma^*_{IF}$) or pnictogen-type (e.g., $n_F \rightarrow \sigma^*_{PR}$) bonding motifs, just as for the dominant $n_B \rightarrow \sigma^*_{HA}$ interaction of B...H—A hydrogen bonding. We obtained evidence both for resonance-type “bond conservation” rules and the complete set of mutually consistent correlations of NBO/NRT descriptors with experimentally measurable properties of RPH₂...IF/Fl complexes that closely parallel those previously demonstrated for H-bonded complexes. We also demonstrate that the removal of $n \rightarrow \sigma^*$ interactions obliterates the signature features of halogen/pnictogen bonding, whereas such features persist (albeit in muted form) even if envisioned “dipole–dipole” contributions are reversed (by reversing dihalogen monomer direction). Thus, our results establish that resonance-type $n \rightarrow \sigma^*$ stabilization is both necessary and sufficient for the characteristic structural, energetic, and spectroscopic features of halogen or pnictogen bonding, as was previously demonstrated for H-bonding [22,23]. The present results are fully consistent with previous studies of orbital-interaction effects in halogen or pnictogen bonding [82,83]. Connections can also be seen to more nuanced interpretation of the “ σ -hole” in terms of chemical “lone pair” interactions with the “extension of one of the covalent bonds,” “dative sharing (coordinate covalence),” and other quantal phenomena [84].

Based on these results, we anticipate that similar unique associations with resonance-type $n \rightarrow \sigma^*$ “fractional bonding” will be found for chalcogen bonds, tetrel bonds, and all other such supramolecular bonding phenomena. Our conclusions thereby extend “resonance covalency” concepts to the entire supramolecular domain of sub-integer bond orders, challenging the common “electrostatic” assumptions that underlie current empirical force field modeling and textbook expositions of supramolecular chemistry.

Supplementary Materials: The following are available online. (1) Optimized geometrical parameters of title species for three alternative basis levels and the dispersion-corrected B3LYP-D3/mix-PP alternative method; (2) graphical displays of RPH₂...Fl complexes compared for all five alternative theory levels; (3) sample input files for NBO, STERIC, and DELETE-type calculations; and (4) optimized coordinates of all dihalogen complexes at the B3LYP/mixed-PP level.

Author Contributions: Conceptualization, Y.J. and F.W.; investigation, Y.J.; writing, Y.J. (draft) and F.W. (final).

Funding: Y.J. acknowledges China Scholarship Council (201808430269) for financial support for visiting UW-Madison and the Natural Science Foundation of Hunan Province (2019JJ50161), China. Support for computational facilities was provided in part by National Science Foundation Grant CHE-0840494.

Conflicts of Interest: The authors declare no conflicts of interest.

References

1. Wolf, M.E.; Zhang, B.Y.; Turney, J.M.; Schaefer, H.F., III. A comparison between hydrogen and halogen bonding: The hypohalous acid–water dimers, HOX...H₂O (X = F, Cl, Br). *Phys. Chem. Chem. Phys.* **2019**, *21*, 6160–6170. [[CrossRef](#)]
2. Chalanchi, S.M.; Alkorta, I.; Elguero, J.; Quinonero, D. Hydrogen bond versus halogen bond in cation-cation complexes: Effect of the solvent. *ChemPhysChem* **2017**, *18*, 3462–3468. [[CrossRef](#)] [[PubMed](#)]
3. Shaw, R.A.; Hill, J.G.; Legon, A.C. Halogen bonding with phosphine: Halogen bonding with phosphine: Evidence for Mulliken inner complexes and the importance of relaxation energy. *J. Phys. Chem. A* **2016**, *120*, 8461–8468. [[CrossRef](#)] [[PubMed](#)]

4. Wang, C.; Fu, Y.; Zhang, L.; Danovich, D.; Shaik, S.; Mo, Y. Hydrogen- and halogen-bonds between ions of like charges: Are they *anti*-electrostatic in nature? *J. Comput. Chem.* **2018**, *39*, 481–487. [[CrossRef](#)] [[PubMed](#)]
5. Matsuzaki, K.; Uno, H.; Tokunaga, E.; Shibata, N. Fluorobissulfonylmethyl iodides: An efficient scaffold for halogen bonding catalysts with an sp³-hybridized carbon–iodine moiety. *ACS Catal.* **2018**, *8*, 6601–6605. [[CrossRef](#)]
6. Legon, A.C. Prereactive complexes of dihalogens XY with Lewis bases B in the gas phase: A systematic case for the halogen analogue B⋯XY of the hydrogen bond B⋯HX. *Angew. Chem. Int. Ed.* **1999**, *38*, 2686–2714. [[CrossRef](#)]
7. Ji, B.M.; Wang, W.Z.; Deng, D.S.; Zhang, Y. Symmetrical bifurcated halogen bond: Design and synthesis. *Cryst. Growth Des.* **2011**, *11*, 3622–3628. [[CrossRef](#)]
8. Henkel, S.; Trosien, I.; Mieres-Pérez, J.; Lohmiller, T.; Savitsky, A.; Sanchez-Garcia, E.; Sander, W. Reactions of cyclopentadienylidenes with CF₃I: Electron bond donation versus halogen bond donation of the iodine atom. *J. Org. Chem.* **2018**, *83*, 7586–7592. [[CrossRef](#)]
9. Cavallo, G.; Metrangolo, P.; Milani, R.; Pilati, T.; Priimagi, A.; Resnati, G.; Terraneo, G. The halogen bond. *Chem. Rev.* **2016**, *116*, 2478–2601. [[CrossRef](#)] [[PubMed](#)]
10. Tawfik, M.; Donald, K.J. Halogen Bonding: Unifying perspectives on organic and inorganic cases. *J. Phys. Chem. A* **2014**, *118*, 10090–10100. [[CrossRef](#)]
11. Quinonero, D.; Alkorta, I.; Elguero, J. Cation–cation and anion–anion complexes stabilized by halogen bonds. *Phys. Chem. Chem. Phys.* **2016**, *18*, 27939–27950. [[CrossRef](#)] [[PubMed](#)]
12. Nunzi, F.; Cesario, D.; Belpassi, L.; Tarantelli, F.; Roncaratti, L.F.; Falcinelli, S.; Cappelletti, D.; Pirani, F. Insight into the halogen-bond nature of noble gas-chlorine systems by molecular beam scattering experiments, ab initio calculations and charge displacement analysis. *Phys. Chem. Chem. Phys.* **2019**, *21*, 7330–7340. [[CrossRef](#)] [[PubMed](#)]
13. Wu, J.Y.; Yan, H.; Zhong, A.G.; Chen, H.; Jin, Y.X.; Dai, G.L. Theoretical and conceptual DFT study of pnictogen- and halogen-bonded complexes of PH₂X⋯BrCl. *J. Mol. Model.* **2019**, *25*, 28. [[CrossRef](#)] [[PubMed](#)]
14. Wang, W.Z.; Ji, B.M.; Zhang, Y. Chalcogen bond: A sister noncovalent bond to halogen bond. *J. Phys. Chem. A* **2009**, *113*, 8132–8135. [[CrossRef](#)] [[PubMed](#)]
15. Kim, Y.; Song, S.; Sim, E. Halogen and chalcogen binding dominated by density-driven errors. *J. Phys. Chem. Lett.* **2019**, *10*, 295–301. [[CrossRef](#)]
16. Scheiner, S. The pnictogen bond: Its relation to hydrogen, halogen, and other noncovalent bonds. *Acc. Chem. Res.* **2013**, *46*, 280–288. [[CrossRef](#)] [[PubMed](#)]
17. Mani, D.; Arunan, E. The X–C⋯Y carbon bond. In *Noncovalent Forces. Challenges and Advances in Computational Chemistry and Physics*; Scheiner, S., Ed.; Springer: New York, NY, USA, 2015; Volume 19.
18. Mani, D.; Arunan, E. The X–C⋯Y (X = O/F, Y = O/S/F/Cl/Br/N/P) ‘carbon bond’ and hydrophobic interactions. *Phys. Chem. Chem. Phys.* **2013**, *15*, 14377–14383. [[CrossRef](#)]
19. Zierkiewicz, W.; Michalczyk, M.; Wysokiński, R.; Scheiner, S. Dual geometry schemes in tetrel bonds: Complexes between TF₄ (T = Si, Ge, Sn) and pyridine derivatives. *Molecules* **2019**, *24*, 376. [[CrossRef](#)]
20. Arunan, E.; Desiraju, G.R.; Klein, R.A.; Sadlej, J.; Scheiner, S.; Alkorta, I.; Clary, D.C.; Crabtree, R.H.; Dannenberg, J.J.; Hobza, P.; et al. Defining the hydrogen bond: An account (IUPAC Technical Report). *Pure Appl. Chem.* **2011**, *83*, 1619–1636. [[CrossRef](#)]
21. Desiraju, G.R.; Ho, P.S.; Kloo, L.; Legon, A.C.; Marquardt, R.; Metrangolo, P.; Politzer, P.; Resnati, G.; Rissanen, K. Definition of the halogen bond (IUPAC Recommendations 2013). *Pure Appl. Chem.* **2013**, *85*, 1711–1713. [[CrossRef](#)]
22. Weinhold, F.; Klein, R.A. What is a hydrogen bond? Mutually consistent theoretical and experimental criteria for characterizing H-bonding interactions. *Mol. Phys.* **2012**, *110*, 565–579. [[CrossRef](#)]
23. Weinhold, F.; Klein, R.A. What is a hydrogen bond? Resonance covalency in the supramolecular domain. *Chem. Educ. Res. Pract.* **2014**, *15*, 276–285. [[CrossRef](#)]
24. Varadwaj, A.; Marques, H.M.; Varadwaj, P.R. Is the fluorine in molecules dispersive? Is molecular electrostatic potential a valid property to explore fluorine-centered non-covalent interactions? *Molecules* **2019**, *24*, 379. [[CrossRef](#)]
25. Weinhold, F.; Landis, C.R.; Glendening, E.D. What is NBO analysis and how is it useful? *Int. Rev. Phys. Chem.* **2016**, *35*, 399–440. [[CrossRef](#)]
26. Stone, A.J. *The Theory of Intermolecular Forces*, 2nd ed.; Oxford University Press: London, England, 2013.

27. Jeziorski, B.; Moszynski, R.; Szalewicz, K. Perturbation theory approach to intermolecular potential energy surfaces of van der Waals complexes. *Chem. Rev.* **1994**, *94*, 1887–1930. [[CrossRef](#)]
28. Chirlan, L.E.; Francl, M.M. Atomic charges derived from electrostatic potentials: A detailed study. *J. Comput. Chem.* **1987**, *8*, 894–905. [[CrossRef](#)]
29. Sigfridsson, E.; Ryde, U. Comparison of methods for deriving atomic charges from the electrostatic potential and moments. *J. Comput. Chem.* **1998**, *19*, 377–395. [[CrossRef](#)]
30. Clark, T.; Hennemann, M.; Murray, J.S.; Politzer, P. Halogen bonding: The sigma-hole. Proceedings of “Modeling interactions in biomolecules II”, Prague, September 5th–9th, 2005. *J. Mol. Model.* **2007**, *13*, 291–296. [[CrossRef](#)] [[PubMed](#)]
31. Clark, T. σ -Holes. *WIREs Comput. Mol. Sic.* **2013**, *3*, 13–20.
32. Stone, A.J. Are halogen bonded structures electrostatically driven? *J. Am. Chem. Soc.* **2013**, *135*, 7005–7009. [[CrossRef](#)]
33. Hermans, J. Hydrogen bonds in molecular mechanics force fields. *Advan. Protein Chem.* **2005**, *72*, 105–119.
34. Rendine, S.; Pieraccini, S.; Forni, A.; Sironi, M. Halogen bonding in ligand–receptor systems in the framework of classical force fields. *Phys. Chem. Chem. Phys.* **2011**, *13*, 19508–19516. [[CrossRef](#)]
35. Grabowski, S.J. Ab initio calculations on conventional and unconventional hydrogen bonds—Study of the hydrogen bond strength. *J. Phys. Chem. A* **2001**, *105*, 10739–10746. [[CrossRef](#)]
36. Grabowski, S.J. What is the covalency of hydrogen bonding? *Chem. Rev.* **2011**, *111*, 2597–2625. [[CrossRef](#)] [[PubMed](#)]
37. Metrangolo, P.; Neukirch, H.; Pilati, T.; Resnati, G. Halogen bonding based recognition processes: A world parallel to hydrogen bonding. *Acc. Chem. Res.* **2005**, *38*, 386–395. [[CrossRef](#)]
38. Quiñonero, D.; Frontera, A. Hydrogen bond versus halogen bond in HXO_n ($X = \text{F, Cl, Br, and I}$) complexes with Lewis bases. *Inorganics* **2019**, *7*, 9. [[CrossRef](#)]
39. Reed, A.E.; Curtiss, L.A.; Weinhold, F. Intermolecular interactions from a natural bond orbital, donor-acceptor viewpoint. *Chem. Rev.* **1988**, *88*, 899–926. [[CrossRef](#)]
40. Glendening, E.D.; Weinhold, F. Natural resonance theory. I. General formulation. *J. Comput. Chem.* **1998**, *19*, 593–609. [[CrossRef](#)]
41. Glendening, E.D.; Weinhold, F. Natural resonance theory. II. Natural bond order and valency. *J. Comput. Chem.* **1998**, *19*, 610–627. [[CrossRef](#)]
42. Glendening, E.D.; Badenhoop, J.K.; Weinhold, F. Natural resonance theory. III. Chemical applications. *J. Comput. Chem.* **1998**, *19*, 628–646. [[CrossRef](#)]
43. Glendening, E.D.; Landis, C.R.; Weinhold, F. Resonance theory reboot. *J. Am. Chem. Soc.* **2019**, *141*, 4156–4166. [[CrossRef](#)]
44. Weinhold, F. Resonance character of hydrogen-bonding interactions in water and other H-bonded species. *Advan. Protein Chem.* **2006**, *72*, 121–155.
45. Coulson, C.A. The nature of the bonding in xenon fluorides and related molecules. *J. Chem. Soc.* **1964**, *1964*, 1442–1454. [[CrossRef](#)]
46. Pimentel, G.C. The bonding of trihalide and bifluoride ions by the molecular orbital method. *J. Chem. Phys.* **1951**, *19*, 446–448. [[CrossRef](#)]
47. Hach, R.J.; Rundle, R.E. The structure of tetramethylammonium pentaiodide. *J. Am. Chem. Soc.* **1951**, *73*, 4321–4324. [[CrossRef](#)]
48. Shahi, A.; Arunan, E. Hydrogen bonding, halogen bonding and lithium bonding: An atoms in molecules and natural bond orbital perspective towards conservation of total bond order, inter- and intra-molecular bonding. *Phys. Chem. Chem. Phys.* **2014**, *16*, 22935–22952. [[CrossRef](#)]
49. Weinhold, F.; Landis, C.R. *Discovering Chemistry with Natural Bond Orbitals*; Wiley: New York, NY, USA, 2012; Section 5.
50. Weinhold, F.; Klein, R.A. Anti-electrostatic hydrogen bonds. *Angew. Chem. Int. Ed.* **2014**, *53*, 11214–11217. [[CrossRef](#)] [[PubMed](#)]
51. Jiao, Y.C.; Liu, Y.; Zhao, W.J.; Wang, Z.X.; Ding, X.L.; Liu, H.X.; Lu, T. Theoretical study on the interactions of halogen-bonds and pnictogen-bonds in phosphine derivatives with Br_2 , BrCl , and BrF . *Int. J. Quantum Chem.* **2017**, *117*, e25443. [[CrossRef](#)]
52. London, F. Zur Theorie und Systematik der Molekularkräfte. *Z. Physik* **1930**, *63*, 245–279. [[CrossRef](#)]

53. Grimme, S. Semiempirical GGA-type density functional constructed with a long-range dispersion correction. *J. Comput. Chem.* **2006**, *27*, 1787–1799. [[CrossRef](#)] [[PubMed](#)]
54. Badenhoop, J.K.; Weinhold, F. Natural bond orbital analysis of steric interactions. *J. Chem. Phys.* **1997**, *107*, 5406–5421. [[CrossRef](#)]
55. Foresman, J.B.; Frisch, A.E. *Exploring Chemistry with Electronic Structure Methods*, 3rd ed.; Gaussian: Wallingford, CT, USA, 2015.
56. Frisch, M.J.; Trucks, G.W.; Schlegel, H.B.; Scuseria, G.E.; Robb, M.A.; Cheeseman, J.R.; Scalmani, G.; Barone, V.; Mennucci, B.; Petersson, G.A.; et al. *Gaussian 16, Revision B.01*; Gaussian Inc.: Wallingford, CT, USA, 2016.
57. Glendening, E.D.; Badenhoop, J.K.; Reed, A.E.; Carpenter, J.E.; Bohmann, J.A.; Morales, C.M.; Karafiloglou, P.; Landis, C.R.; Weinhold, F. *NBO 7.0*; Theoretical Chemistry Institute, University Wisconsin: Madison, WI, USA, 2018.
58. Weinhold, F.; Phillips, D.; Foo, Z.Y.; Glendening, E.D.; Hanson, R.M. *NBOPro@Jmol*; Theoretical Chemistry Institute, University Wisconsin: Madison, WI, USA, 2018.
59. Pauling, L. *The Nature of the Chemical Bond*, 2nd ed.; Cornell University Press: Ithaca, NY, USA, 1940; p. 189.
60. Weinhold, F.; Landis, C.R. *Valency and Bonding: A Natural Bond Orbital Donor-Acceptor Perspective*; Cambridge University Press: Cambridge, UK, 2005; Section 5.2.
61. Reed, A.E.; Weinhold, F. Natural bond orbital analysis of near-Hartree-Fock water dimer. *J. Chem. Phys.* **1983**, *78*, 4066–4073. [[CrossRef](#)]
62. Curtiss, L.A.; Pochatko, D.J.; Reed, A.E.; Weinhold, F. Investigation of the differences in stability of the OCHF and COHF complexes. *J. Chem. Phys.* **1985**, *82*, 2679–2687. [[CrossRef](#)]
63. Reed, A.E.; Weinhold, F. Natural bond orbital analysis of molecular interactions: Theoretical studies of binary complexes of HF, H₂O, NH₃, N₂, O₂, F₂, CO, and CO₂ with HF, H₂O, and NH₃. *J. Chem. Phys.* **1986**, *84*, 5687–5705. [[CrossRef](#)]
64. Sidgwick, N.V. *The Electronic Theory of Valency*; Oxford University Press: London, UK, 1929; p. 72, 147f.
65. Pimentel, G.C.; McClellan, A.L. Hydrogen bonding. *Annu. Rev. Phys. Chem.* **1971**, *22*, 347–385. [[CrossRef](#)]
66. Ratajczak, H. Charge-transfer properties of the hydrogen bond. I. Theory of the enhancement of dipole moment of hydrogen-bonded systems. *J. Phys. Chem.* **1972**, *76*, 3000–3004. [[CrossRef](#)]
67. Baiocchi, F.; Reiher, W.; Klemperer, W. Comments on “Do electrostatic interactions predict structure of van der Waals molecules?”. *J. Chem. Phys.* **1983**, *79*, 6428–6429. [[CrossRef](#)]
68. Ronca, E.; Belpassi, L.; Tarantelli, F. A quantitative view of charge transfer in the hydrogen bond: The water dimer case. *ChemPhysChem* **2014**, *15*, 2682–2687. [[CrossRef](#)]
69. Mulliken, R.S. Overlap integrals and chemical binding. *J. Am. Chem. Soc.* **1950**, *72*, 4493–4503. [[CrossRef](#)]
70. Wolfsberg, M.; Helmholz, L.J. The spectra and electronic structure of the tetrahedral ions MnO₄[−], CrO₄[−], and ClO₄[−]. *J. Chem. Phys.* **1952**, *20*, 837–843. [[CrossRef](#)]
71. Hoffmann, R. An extended Hückel Theory I. Hydrocarbons. *J. Chem. Phys.* **1963**, *39*, 1397–1412. [[CrossRef](#)]
72. Hoffmann, R.; Lipscomb, W.N. Boron hydrides: LCAO-MO and resonance studies. *J. Chem. Phys.* **1962**, *37*, 2872–2883. [[CrossRef](#)]
73. Weinhold, F.; Landis, C.R. *Discovering Chemistry with Natural Bond Orbitals*; Wiley: New York, NY, USA, 2012; p. 63.
74. Löwdin, P.-O. Quantum theory of many-particle systems. I. Physical interpretations by means of density matrices, natural spin-orbitals, and convergence problems in the method of configurational interaction. *Phys. Rev.* **1955**, *97*, 1474–1489. [[CrossRef](#)]
75. Glendening, E.D.; Wright, S.J.; Weinhold, F. Efficient optimization of natural resonance theory weightings with convex programming. *J. Comput. Chem.* **2019**. [[CrossRef](#)]
76. Landis, C.R.; Weinhold, F. 3c/4eδ-type long-bonding: A novel NBO motif toward the metallic delocalization limit. *Inorg. Chem.* **2013**, *52*, 5154–5166. [[CrossRef](#)]
77. Zhang, G.Q.; Li, H.; Weinhold, F.; Chen, D.Z. 3c/4eδ-type long-bonding competes with x-bonding in noble-gas hydrides HNgY (Ng = He, Ne, Ar, Kr, Xe, Rn; Y = F, Cl, Br, I): A NBO/NRT perspective. *Phys. Chem. Chem. Phys.* **2016**, *18*, 8015–8026. [[CrossRef](#)] [[PubMed](#)]
78. Zhang, G.Q.; Zhang, S.N.; Chen, D.Z. Long-bonding in HNgCN/NC (Ng = Noble Gas) molecules: An NBO/NRT investigation. *J. Phys. Chem. A* **2017**, *121*, 5524–5532. [[CrossRef](#)] [[PubMed](#)]
79. Coulson, C.A. The electronic structure of some polyenes and aromatic molecules. VII. Bonds of fractional order by the molecular orbital method. *Proc. R. Soc. London A* **1939**, *169*, 413–428.

80. Johnston, H.S. Large tunneling corrections in chemical reaction rates. *Adv. Chem. Phys.* **1960**, *3*, 131–170.
81. Badger, R.M. The relation between the internuclear distances and force constants of molecules and its application to polyatomic molecules. *J. Chem. Phys.* **1935**, *3*, 710–714. [[CrossRef](#)]
82. Grabowski, S.J. Hydrogen and halogen bonds are ruled by the same mechanisms. *Phys. Chem. Chem. Phys.* **2013**, *15*, 7249–7259. [[CrossRef](#)] [[PubMed](#)]
83. Alkorta, I.; Elguero, J.; Grabowski, S.J. Nitrogen and hydrogen bonds; complexes between PH_3X^+ and PH_2X systems. *Phys. Chem. Chem. Phys.* **2015**, *17*, 3261–3272. [[CrossRef](#)]
84. Politzer, P.; Murray, J.S.; Clark, T. Halogen bonding and other σ -hole interactions: A perspective. *Phys. Chem. Chem. Phys.* **2013**, *15*, 11178–11189. [[CrossRef](#)]



© 2019 by the authors. Licensee MDPI, Basel, Switzerland. This article is an open access article distributed under the terms and conditions of the Creative Commons Attribution (CC BY) license (<http://creativecommons.org/licenses/by/4.0/>).